Hyperspectral face recognition for homeland security

Zhihong Pan, Glenn Healey, Manish Prasad, Bruce Tromberg[a]

Department of Electrical Engineering and Computer Science
[a]Beckman Laser Institute
University of California, Irvine, CA

ABSTRACT

Hyperspectral sensors provide useful discriminants for human face recognition that cannot be obtained by other imaging methods. Near-infrared spectral measurements allow the sensing of subsurface tissue structure which is significantly different from person to person but relatively stable over time. The spectral properties of human tissue are also nearly invariant to changes in face orientation which bring significant degradation to most other face recognition algorithms. We examine the utility of using near-infrared hyperspectral images for the recognition of human subjects over a database of 200 subjects. The face recognition algorithm exploits spectral measurements for individual facial tissue types and combinations of facial tissue types. We demonstrate experimentally that hyperspectral imaging promises to support face recognition independent of facial expression and orientation.

1. INTRODUCTION

Various biometric identification technologies based on cues such as fingerprint, voice, and face provide the potential for reliable automatic verification.[1] After 9/11, biometric identification techniques have gained notice as methods which can contribute significantly to the war against terrorism. For applications such as homeland security, we would benefit from a face recognition capability which is fast, accurate, and reliable. Ideally, a face recognition system will identify human subjects under unconstrained conditions, including unknown illumination, arbitrary face orientation, and partial face occlusion. Such as system should also be capable of operating with a significant distance between the camera and the subject.

Current face recognition systems use primarily spatial discriminants that are based on geometric facial features.[2–6] Many of these systems have performed well on databases acquired under controlled conditions.[7] However, these approaches often exhibit significant performance degradation in the presence of changes in face orientation. One study,[8] for example, showed that there is significant degradation in recognition performance for images of faces that are rotated more than 32° from a frontal image that is used to train the system. A more recent study[9] which uses a light-fields model for pose-invariant face recognition showed promising results on faces rotated more than 60°. Algorithms that use geometric features can also perform poorly when subjects are imaged at different times. For example, recognition performance can degrade by as much as 20% when imaging sessions are separated by a two week interval.[8] Partial face occlusion also brings poor performance. A method[10] that divides the face into regions for isolated analysis can tolerate up to 1/6 face occlusion without losing accuracy. Thermal infrared imaging provides an alternative imaging modality that has been used for face recognition.[11, 12] However, thermal imaging techniques use spatial features and have difficulty recognizing faces after pose changes. A 3D morphable face model has been used for face identification across different poses.[13] This approach has provided promising performance on a 68 subject dataset. At the current time, however, this system is computationally intensive and requires considerable manual intervention.

Spectroscopy, which represents the spectral distribution of light that is reflected and scattered from an object, is a valuable tool for a large number of applications. In remote sensing, for example, researchers have shown that hyperspectral data are effective for material identification in scenes where other sensing modalities are ineffective.[14] Before the introduction of hyperspectral images, however, spectroscopy was limited to measuring

Further author information: (Send correspondence to G. Healey)
G. Healey: E-mail: healey@ece.uci.edu; Z. Pan: E-mail: zpan@ece.uci.edu

Infrared Technology and Applications XXIX, Bjørn F. Andresen, Gabor F. Fulop, Editors,
Proceedings of SPIE Vol. 5074 (2003) © 2003 SPIE · 0277-786X/03/$15.00

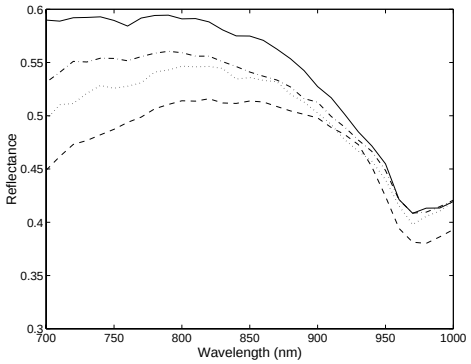

Figure 1: Skin spectra for 4 subjects

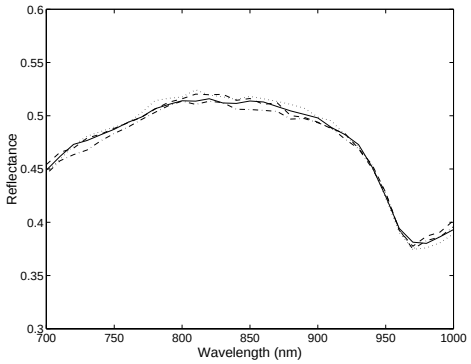

Figure 2: Four skin spectra for one subject

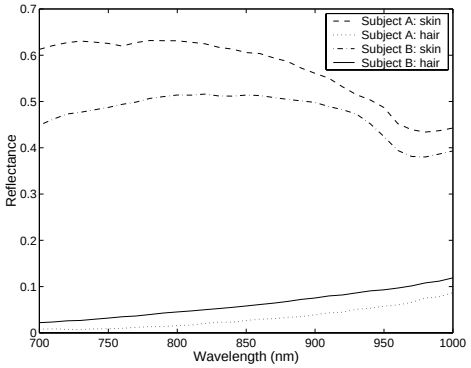

Figure 3. Skin and hair reflectance spectra for two subjects - front view

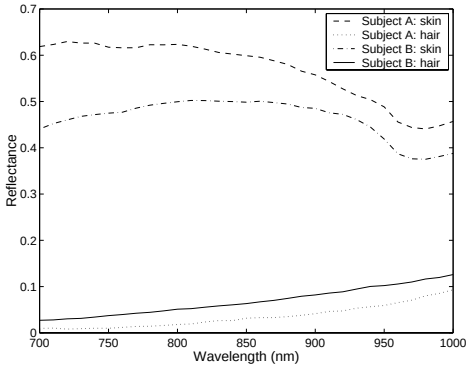

Figure 4. Skin and hair reflectance spectra for two subjects - 90° side view

isolated points. As hyperspectral cameras have become economically accessible, computational methods have been developed for several applications[15,16] using combinations of spectral and spatial information.

Several of the limitations of current face recognition systems can be overcome by using spectral information of human face tissue. The interaction of light with human tissue has been studied extensively by various researchers.[17–19] It is known that the surface reflection of the skin at the air-tissue interface is only around $4\% - 7\%$ over the 250nm-3000nm spectral range[20] and that the incident radiation is diffused by the stratum corneum before entering the epidermal layer. The epidermal and dermal layers of human skin constitute the major scattering medium which, together with the light-absorbing chromophores, such as melanin, hemoglobin, bilirubin, and β-carotene, determines the skin's spectral reflectance. Small changes in the chromophore concentrations induce significant changes in the reflectance.[21] The effects are large enough, for example, to enable algorithms for the automated separation of melanin and hemoglobin from RGB images.[22] Multispectral skin color models over the visible range have been studied for applications such as human detection, face tracking, and computer graphics.[23,24] In the near-infrared (NIR), skin has a significant penetration depth enabling the imaging of subsurface characteristics that are difficult for a person to modify.[25]

Figure 1 presents an example of the spectral variability in human skin using measurements obtained at our laboratory. It includes the reflectance spectra measured from the right cheek of four subjects over the near-infrared (700nm-1000nm). In figure 2, four reflectance spectra were acquired for one subject from different facial locations. We see that there are significant differences in both the amplitude and spectral shape for different subjects while the spectral reflectance for one subject remains similar from trial-to-trial. Spectral variation for a single subject is also typically small over a range of poses. In figure 3, near-infrared skin and hair reflectance

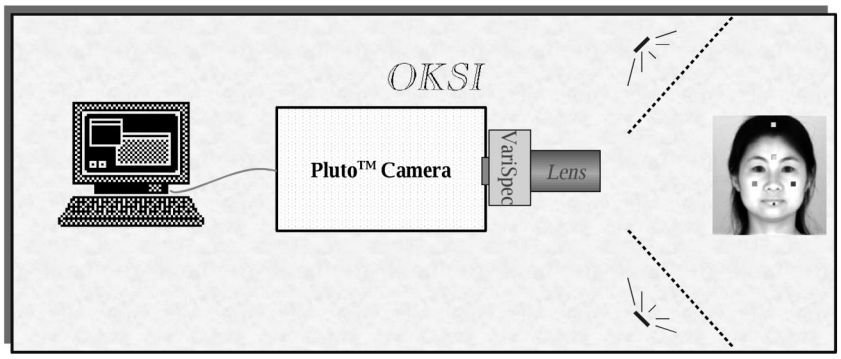

Figure 5: Hyperspectral imaging system set-up

Figure 6: Thirty-one bands for a hyperspectral image of one subject

spectra are plotted for two subjects as acquired in a front-view hyperspectral image. In figure 4, reflectance spectra for the same subjects are plotted as acquired in a side-view (profile) image. We see that while there is significant spectral variability from one subject to the other, the spectral characteristics of the subjects remain stable over a large change in face orientation.

In this paper, we consider the use of spectral information for face recognition. We present experimental results on recognizing 200 human subjects using hyperspectral face images. For each subject, several near-infrared images were acquired under different poses and expression. Recognition is achieved by combining spectral measurements for different tissue types. Some subjects were imaged multiple times over several weeks to evaluate the stability of the hyperspectral measurements over time.

2. DATA COLLECTION AND CAMERA CALIBRATION

The hyperspectral imaging system utilized for data collection is configured as in figure 5. The hyperspectral camera from Opto-Knowledge Systems, Inc. (OKSI) is based on a liquid crystal tunable filter[26] made by Cambridge Research Instruments (CRI). The full-width at half-maximum (FWHM) of the spectral bands is 10nm for a center wavelength of 850nm and is proportional to the center wavelength squared. The locations of the camera, the diffused light sources, and the stage where the subject sits were all fixed throughout the data collection period. All images were captured with 31 bands spaced by 0.01μm over the near-infrared (0.7μm-1.0μm) with 468×494 spatial resolution. A hyperspectral image of 31 bands takes about 10 seconds to acquire.

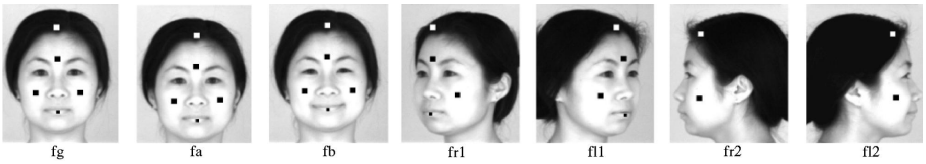

Figure 7: Examples of images with different expressions and rotations

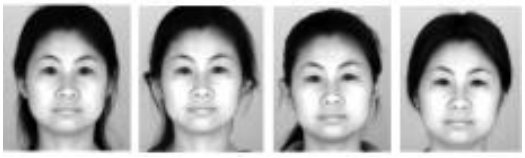

Figure 8: Examples of images taken at different times

Figure 6 displays all 31 bands for one subject. The 31 bands are shown in ascending order from left to right and from top to bottom.

The spectral channels have unknown gains due to filter transmission and CCD response and unknown offsets due to dark current and stray light. Therefore, we devised a method to convert the raw images acquired by the hyperspectral camera to spectral reflectance images for analysis.[16] Two spectralon panels were used during calibration. A panel with approximately 99% reflectance is referred to as white spectralon and a panel with approximately 2% reflectance is referred to as black spectralon.

The raw measurement obtained by the hyperspectral imaging system at spatial coordinate (x, y) and wavelength λ_k is given by

$$I(x, y, \lambda_k) = L(x, y, \lambda_k)S(x, y, \lambda_k)R(x, y, \lambda_k) + O(x, y, \lambda_k) \tag{1}$$

where $L(x, y, \lambda_k)$ is the illumination, $S(x, y, \lambda_k)$ is the system spectral response, $R(x, y, \lambda_k)$ is the reflectance of the viewed surface, and $O(x, y, \lambda_k)$ is the offset which includes dark current and stray light. To obtain the spectral reflectance image $R(x, y, \lambda_k)$, we take hyperspectral images of the white and black spectralon to get the raw measurements $I_W(x, y, \lambda_k)$ and $I_B(x, y, \lambda_k)$ respectively. Both measurements are averaged over 10 images. With the averaged I_W and I_B, we can calibrate to reflectance[16] using

$$R(x, y, \lambda_k) = \frac{(I(x, y, \lambda_k) - I_B(x, y, \lambda_k))R_W(\lambda_k)}{I_W(x, y, \lambda_k) - I_B(x, y, \lambda_k)} + \frac{(I_W(x, y, \lambda_k) - I(x, y, \lambda_k))R_B(\lambda_k)}{I_W(x, y, \lambda_k) - I_B(x, y, \lambda_k)} \tag{2}$$

We measured I_W and I_B at the beginning of each imaging session. After calibration, the reflectance spectrum will be invariant to illumination, although we keep the illumination fixed for different imaging sessions.

We collected hyperspectral face images of 200 human subjects. Images of all human subjects were acquired in sets of seven images per subject. Figure 7 shows the seven images for one subject. Two front-view images were taken with neutral expression (fg and fa). Another front-view image fb was taken with a different expression. Four other images were taken with face orientations of -90°, -45°, 45°, and 90°, which are referred to as fr2, fr1, fl1 and fl2 respectively. Twenty of the 200 subjects were imaged at different times separated by up to five weeks from their initial imaging session. Figure 8 shows the front-view images of one subject taken at four different visits.

3. SPECTRAL METRIC FOR FACE RECOGNITION

In order to test the feasibility of hyperspectral face recognition, we represent each face image using spectral reflectance vectors that are extracted from small facial regions. Squares overlayed on the images in figure 7 indicate the size and location of the regions that are considered for each subject. For the frontal images (fg,fa,fb), five facial regions corresponding to the forehead, left cheek, right cheek, hair, and lips are used. For images

acquired at other facial orientations, the subset of these facial regions that are visible are used as shown in figure 7. The forehead, for example, is not visible for a facial orientation of 90°.

For each facial region, the spectral reflectance vector $\mathbf{R}_t = (R_t(\lambda_1), R_t(\lambda_2) \cdots, R_t(\lambda_B))^T$ is estimated by averaging over the N pixel squares shown in figure 7 according to

$$R_t(\lambda_k) = \frac{1}{N} \sum_{x,y} R(x, y, \lambda_k) \qquad k = 1, 2, \ldots, B \tag{3}$$

where the sum is over the N pixels in the square, B is the number of spectral bands, and t is one of the following tissue types: f(forehead), lc(left cheek), rc(right cheek), h(hair), or l(lip). The normalized spectral reflectance vector $\overline{\mathbf{R}}_t$ is defined by

$$\overline{\mathbf{R}}_t = \mathbf{R}_t / \|\mathbf{R_t}\| \tag{4}$$

The distance between face image i and face image j for tissue type t is defined by the square of the Mahalanobis distance[27]

$$D'_t(i, j) = \left(\overline{\mathbf{R}}_t(i) - \overline{\mathbf{R}}_t(j)\right)^T \Sigma_t^{-1} \left(\overline{\mathbf{R}}_t(i) - \overline{\mathbf{R}}_t(j)\right) \tag{5}$$

where Σ_t is the covariance matrix for the distribution of the vector $\overline{\mathbf{R}}_t$ for a subject. Note that we are using a single Σ_t to represent variability for tissue type t over the entire database. Since the amount of data available to estimate the covariance matrix is limited, we approximate Σ_t by a diagonal matrix L_t with elements that correspond to the variance at each λ_k. The matrix $L_t(i)$ is estimated for each subject i using the vectors $\overline{\mathbf{R}}_t(i)$ from each image of subject i that contains tissue type t. The overall matrix L_t which is used to approximate Σ_t in (5) is obtained by averaging the $L_t(i)$ matrices over all subjects. Figure 9 plots the diagonal elements of L_t as a function of wavelength for the forehead tissue type. The corresponding functions for the left cheek and right cheek are similar while the functions for lips and hair have a similar shape but a larger variance. We note that the variance has larger values at the low and high ends of the 700-1000 nm wavelength range. This is due primarily to a lower signal-to-noise ratio for the sensing system for wavelengths near the ends of the spectral range.

Since tissue spectral reflectance can have spatial variability, the distance $D'_t(i, j)$ will have some dependence on the locations of the squares used to compute $\overline{\mathbf{R}}_t(i)$ and $\overline{\mathbf{R}}_t(j)$. We address this issue by defining a set $S_t(i) = \{\overline{\mathbf{R}}_t^{(1)}(i), \overline{\mathbf{R}}_t^{(2)}(i), \ldots, \overline{\mathbf{R}}_t^{(M)}(i)\}$ of normalized spectral reflectance vectors where each $\overline{\mathbf{R}}_t^{(k)}(i)$ is derived from a different N-pixel square region in the image of subject i for tissue type t. A similar set $S_t(j)$ is defined for subject j. The distance $D_t(i, j)$ is now defined as the smallest squared Mahalanobis distance between an element of $S_t(i)$ and an element of $S_t(j)$

$$D_t(i, j) = \min_{k \in [1,M], l \in [1,M]} \left[\left(\overline{\mathbf{R}}_t^{(k)}(i) - \overline{\mathbf{R}}_t^{(l)}(j)\right)^T \Sigma_t^{-1} \left(\overline{\mathbf{R}}_t^{(k)}(i) - \overline{\mathbf{R}}_t^{(l)}(j)\right) \right] \tag{6}$$

In our experiments, we consider $M = 5$ adjacent square regions of size 17×17 pixels arranged in a cross pattern to define the sets $S_t(i)$ for each tissue type except the lips. Smaller regions of size 9×9 pixels are used to represent the smaller spatial extent of the lips.

Recognition performance can be enhanced by utilizing all visible tissue types. Thus, the distance between a frontal face image i and a test face image j is defined as

$$D(i, j) = \omega_f D_f(i, j) + \omega_{lc} D_{lc}(i, j) + \omega_{rc} D_{rc}(i, j) + \omega_h D_h(i, j) + \omega_l D_l(i, j) \tag{7}$$

where ω_t is 1 if tissue type t is visible in the test image and 0 otherwise.

For the analysis above, we have assumed that the calibrated normalized reflectance spectra are invariant to face orientation. This assumption may not be correct for large face rotations. In figure 10, three normalized forehead reflectance spectra for a single subject are plotted together. It is clear that while the two spectra with a 45° face rotation are similar, they deviate from the front view spectrum. Specifically, the spectra of the rotated face tend to be flatter than the front view spectrum. Therefore, we can adjust the spectra of faces

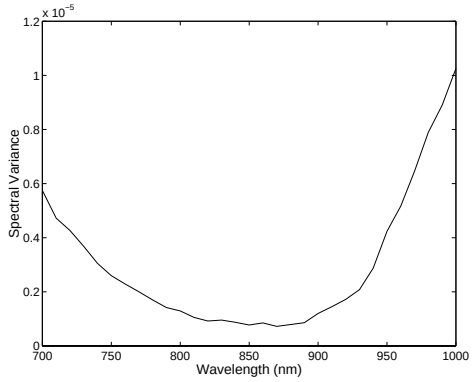

Figure 9. Forehead spectral variance as a function of wavelength

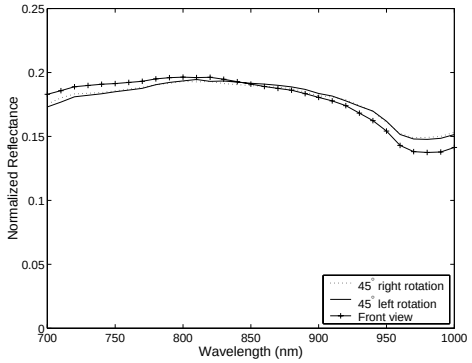

Figure 10. Normalized forehead reflectance spectra of one subject

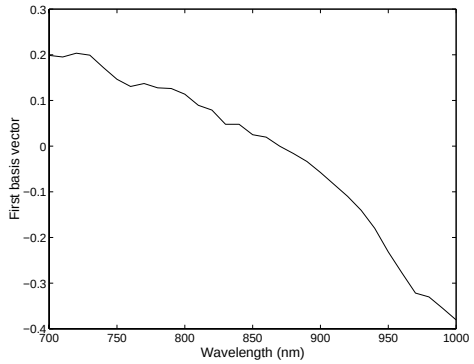

Figure 11. First basis vector of forehead spectral variation due to face orientation

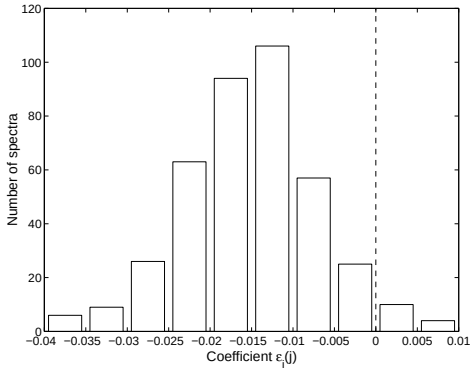

Figure 12. Histogram of $\epsilon_1(j)$ for 400 forehead spectra

rotated 45° or 90° using singular value decomposition (SVD)[28] techniques. Figures 11 and 12 illustrate this method for forehead reflectance spectra with a 45° face rotation. For each of the C subjects, we consider 3 normalized spectral reflectance vectors: $\overline{\mathbf{R}}_f^0(i)$ for the front view forehead spectrum, $\overline{\mathbf{R}}_f^1(i)$ and $\overline{\mathbf{R}}_f^2(i)$ for 45° right and left face rotations respectively. We can get $2C$ spectral variation vectors $\mathbf{V}(j)$ defined by

$$\mathbf{V}(j) = \overline{\mathbf{R}}_f^1(j) - \overline{\mathbf{R}}_f^0(j) \qquad j = 1, 2, \ldots, C \tag{8}$$

$$\mathbf{V}(j+C) = \overline{\mathbf{R}}_f^2(j) - \overline{\mathbf{R}}_f^0(j) \qquad j = 1, 2, \ldots, C \tag{9}$$

Applying the SVD to these $2C$ spectral variation vectors we can generate an orthonormal set of basis vectors $\mathbf{L}_1, \mathbf{L}_2, \ldots, \mathbf{L}_B$ which characterize the spectral variation vectors. The basis vector $\mathbf{L}_1$ that captures the most variation is shown in figure 11. We can approximate the spectral variation by

$$\mathbf{V}(j) = \sum_{b=1}^{B} \epsilon_b(j)\mathbf{L}_b \approx \epsilon_1(j)\mathbf{L}_1 \tag{10}$$

where the coefficients $\epsilon_b(j)$ that minimize the least square error are defined by

$$\epsilon_b(j) = \mathbf{V}(j) \cdot \mathbf{L}_b \tag{11}$$

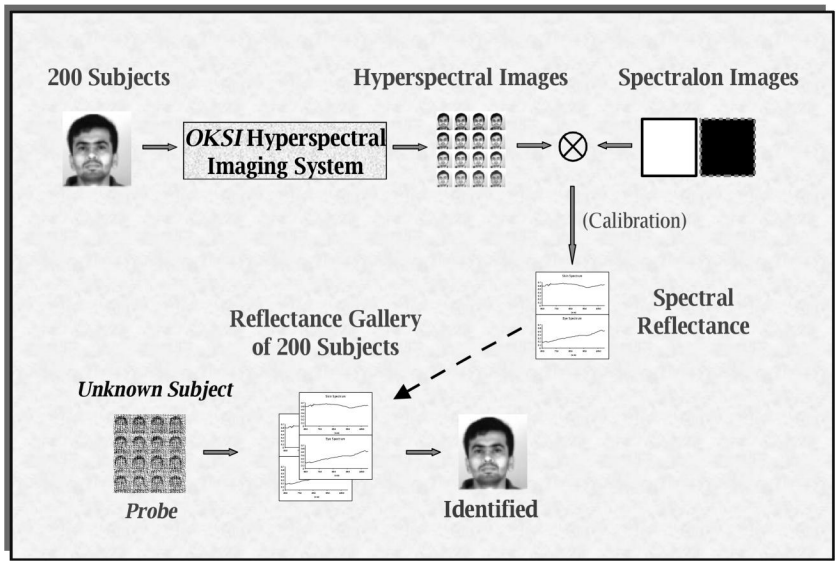

Figure 13: Face recognition system data flow diagram

Figure 12 is the histogram of $\epsilon_1(j)$ for the 200 subjects. Since most coefficients $\epsilon_1(j)$ are negative, we conclude that the forehead reflectance spectra of faces rotated 45° are typically flatter than the front view spectra. To account for this variation, we adjust each 45° spectrum as

$$\hat{\mathbf{R}}_f^1(i) = \overline{\mathbf{R}}_f^1(i) - \epsilon_1 \mathbf{L}_1 \quad (12)$$

$$\hat{\mathbf{R}}_f^2(i) = \overline{\mathbf{R}}_f^2(i) - \epsilon_1 \mathbf{L}_1 \quad (13)$$

where ϵ_1 is the average of the $\epsilon_1(j)$. Thus, $\hat{\mathbf{R}}_f^1(i)$ is a prediction for the spectrum that would be measured for a front view of the patch of skin that generated the spectrum $\overline{\mathbf{R}}_f^1(i)$ from a 45° view. For other tissue types as well as other face rotations, similar adjustments are utilized.

4. EXPERIMENTAL RESULTS

We conducted a series of recognition experiments using an image database consisting of $C = 200$ subjects according to the flow diagram fo figure 13. At each imaging session, seven images of each subject were acquired as shown in figure 7. The images then were calibrated to generate the spectral reflectance images. Image fg is used to represent the subject in the *gallery* set which is the group of hyperspectral images of known identity.[7] The remaining images are used as *probes* to test the recognition algorithm. Thus, the experiments follow the *closed universe* model[7] where the subject in every image in the probe set is present in the gallery.

The results of the experiments will be presented using cumulative match scores.[7] For a probe image j, the image in the gallery which corresponds to the same subject is denoted by T_j. Given a probe image j we can compute $D(i,j)$ for each of the C images i in the gallery. Probe j is correctly recognized if $D(T_j,j)$ is the smallest of the C distances. Given a set of probes, the total number of correctly recognized probes is denoted as M_1. Similarly, M_n is the number of probes for which $D(T_j,j)$ is one of the n smallest of the C distances. The cumulative match score function for an experiment is defined by $R_n = M_n/P$ where P is the total number of probes used in the experiment.

We first consider the use of the frontal fa and fb probes to examine the utility of the various tissue types for hyperspectral face recognition. Figure 14 presents the cumulative match scores as a function of the rank n that are obtained when using $D_t(i,j)$ for each of the tissue types individually and $D(i,j)$ for the combination

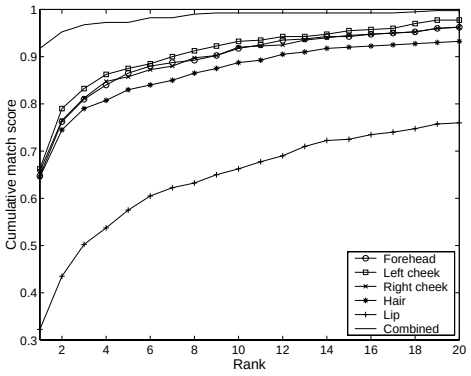

Figure 14. Identification performance using fa and fb probes

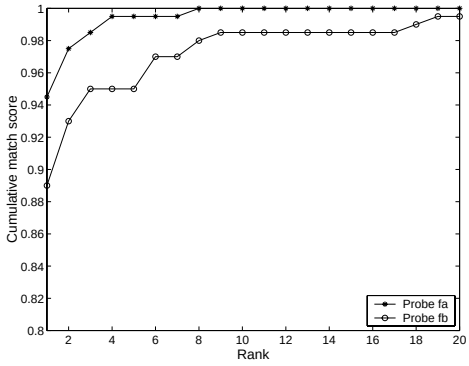

Figure 15. Performance comparison of probe fa and fb

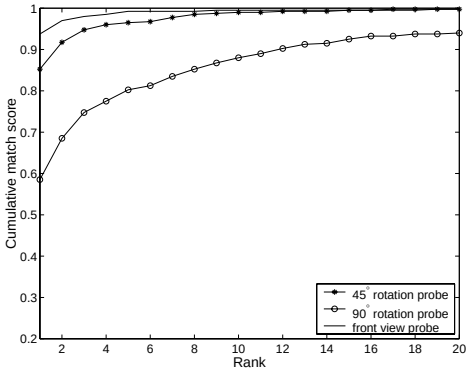

Figure 16. Identification performance of rotated face images

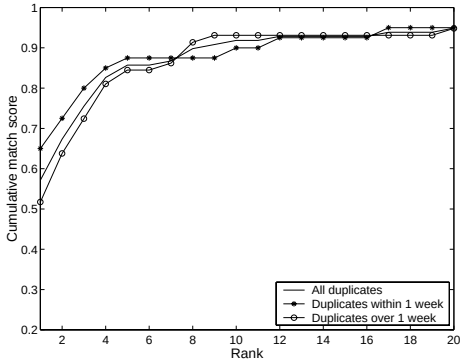

Figure 17. Identification performance of duplicate probes

of all tissue types. We see that skin is the most useful tissue type for recognition while the hair and lips are less useful. The top curve in figure 14 shows that the best performance is achieved by combining all of the tissue types. We see that for this case, over 90% of the probes are correctly identified in the 200 subject database. Figure 15 compares recognition performance when using probes fa and fb separately with the algorithm that considers all tissue types. The fa images have the same facial expression as the gallery images while the fb images have different expressions. We see that accurate recognition is achieved in both cases which suggests that recognition using hyperspectral discriminants is not impacted significantly by changes in facial expression. Nevertheless, probes with different facial expressions are somewhat harder to identify.

Figure 16 examines the impact of changes in face orientation on recognition performance. Most current face recognition systems experience significant difficulty in recognizing probes that differ from a frontal gallery image by more than $32°$.[8] As expected, however, hyperspectral images can be used to achieve accurate recognition results for larger rotations. In figure 16 we see that for probes that are rotated $45°$ to the left or right from the frontal gallery image, 85% of the probes are recognized correctly and 97% of the probes have the correct match ranked in the top 5. For the difficult case of probes that are rotated $90°$, about 87% of the probes have the correct match ranked in the top 10. These results utilize the distance function defined in terms of all visible tissue types.

Figure 17 shows the recognition performance for duplicate probes, i.e. probe images taken on different days than the gallery image of the same subject. This experiment considers 98 probes acquired from 20 subjects at

times between three days and five weeks after the gallery image was acquired. The same 200 subject gallery is used as in the other experiments. We see that 92% of the probes have the correct match ranked in the top 10. Figure 17 also compares the recognition performance for duplicate probes acquired over different time intervals. We see that performance for duplicates acquired within one week (40 probes) is similar to performance for duplicates acquired at an interval of over one week (58 probes). This experiment indicates that hyperspectral imaging has potential for face recognition over time.

5. CONCLUSION

We have demonstrated the utility of hyperspectral imaging for face recognition over time in the presence of changes in head pose and facial expression. The experiments consider a database of calibrated near-infrared (0.7μm-1.0μm) hyperspectral images for 200 subjects. A face recognition algorithm based on the spectral comparison of combinations of tissue types was applied to the images. The results showed that the algorithm performs significantly better than current face recognition systems for identifying rotated faces. The algorithm also provides accurate recognition performance for expression changes and the potential is promising for images acquired over several week time intervals. Since the algorithm uses only local spectral information, we expect that additional performance gains can be achieved by incorporating spatial information into the recognition process. Previous work[14] has shown that the high-dimensionality of hyperspectral data supports the use of subspace methods for illumination-invariant recognition. A similar method may be useful for hyperspectral face recognition under unknown illumination.

ACKNOWLEDGMENTS

This work has been supported by the DARPA Human Identification at a Distance Program through AFOSR Grant F49620-01-1-0058. The experiments were carried out at the Beckman Laser Institute on the UC Irvine campus.

REFERENCES

1. M. Zhang, D. Zhou, Q. Pan, H. Zhang, and S. Zhang, "Biometrics identification techniques," in *Proceedings of 4th World Congress on Intelligent Control and Automation*, pp. 1133–1137, (Shanghai), 2002.
2. K. Etemad and R. Chellappa, "Discriminant analysis for recognition of human face images," *J. Opt. Soc. Am. A* **14**, pp. 1,724–1,733, 1997.
3. B. Moghaddam and A. Pentland, "Probabalistic visual recognition for object recognition," *IEEE Trans. Pattern Anal. Machine Intell.* **19**, pp. 696–710, July 1997.
4. D. Swets and J. Weng, "Using discriminant eigenfeatures for image retrieval," *IEEE Trans. Pattern Anal. Machine Intell.* **18**, pp. 831–836, August 1996.
5. J. Wilder, "Face recognition using transform coding of grayscale projection and the neural tree network," in *Artifical neural networks with applications in speech and vision*, R. Mammone, ed., pp. 520–536, Chapman Hall, 1994.
6. L. Wiskott, J.-M. Fellous, N. Kruger, and C. von der Malsburg, "Face recognition by elastic bunch graph matching," *IEEE Trans. Pattern Anal. Machine Intell.* **19**, pp. 775–779, July 1997.
7. P. Phillips, H. Moon, A. Rizvi, and P. Rauss, "The FERET evaluation methodology for face-recognition algorithms," *IEEE Trans. Pattern Anal. Machine Intell.* **22**, pp. 1090–1104, October 2000.
8. R. Gross, J. Shi, and J. Cohn, "Quo vadis face recognition?," Tech. Rep. CMU-RI-TR-01-17, Robotics Institute, Carnegie-Mellon University, June 2001.
9. R. Gross, I. Matthews, and S. Baker, "Appearance based face recognition and light-fields," Tech. Rep. CMU-RI-TR-02-20, Robotics Institute, Carnegie-Mellon University, August 2002.
10. A. Martínez, "Recognizing imprecisely localized, partially occluded and expression variant faces from a single sample per class," *IEEE Trans. Pattern Anal. Machine Intell.* **24**(6), pp. 748–763, 2002.
11. D. Socolinsky and A. Selinger, "A comparative analysis of face recognition performance with visible and thermal infrared imagery," in *Proc. Int. Conf. on Patt. Recog.*, (Quebec), 2002.

12. J. Wilder, P. Phillips, C. Jiang, and S. Wiener, "Comparison of visible and infra-red imagery for face recognition," in *Proc. IEEE Int. Conf. on Automat. Face and Gesture Recog.*, pp. 182–187, 1996.
13. V. Blanz, S. Romdhani, and T. Vetter, "Face identification across different poses and illuminations with a 3D morphable model," in *Proc. IEEE Int. Conf. on Automat. Face and Gesture Recog.*, pp. 202–207, (Washington, DC), 2002.
14. G. Healey and D. Slater, "Models and methods for automated material identification in hyperspectral imagery acquired under unknown illumination and atmospheric conditions," *IEEE Trans. Geosci. Remote Sensing* **37**, pp. 2706–2717, November 1999.
15. P. Dwyer and C. Dimarzio, "Hyperspectral imaging for dermal hemoglobin spectroscopy," in *SPIE Proceedings Vol. 3752, Subsurface Sensors and Applications*, pp. 72–82, 1999.
16. Z. Pan, M. Prasad, G. Healey, and B. Tromberg, "Recognizing faces in hyperspectral images," in *SPIE Proceedings Vol. 4725, Algorithms for Multispectral, Hyperspectral, and Ultraspectral Imagery VIII*, pp. 168–176, April 2002.
17. R. Anderson and J. Parrish, "The optics of human skin," *Journal of Investigative Dermatology* **77**(1), pp. 13–19, 1981.
18. V. Tuchin, *Tissue Optics: light scattering methods and instruments for medical diagnosis*, SPIE Press, Bellingham, WA, 2000.
19. M. van Gemert, S. Jacques, H. Sternborg, and W. Star, "Skin optics," *IEEE Trans. Biomed. Eng.* **36**, pp. 1146–1154, December 1989.
20. T. Anderson, *An Introduction to Multivariate Statistical Analysis*, Wiley, New York, 1958.
21. E. Edwards and S. Duntley, "The pigments and color of living human skin," *Am. J. Anat.* **65**, pp. 1–33, 1939.
22. N. Tsumura, H. Haneishi, and Y. Miyake, "Independent-component analysis of skin color image," *J. Opt. Soc. Am. A* **16**(9), pp. 2169–2176, 1999.
23. E. Angelopoulou, R. Molana, and K. Daniilidis, "Multispectral skin color modeling," in *Proc. IEEE Conf. on Comp. Vision and Patt. Recog.*, **2**, pp. 635–642, 2002.
24. M. Störring, H. Andersen, and E. Granum, "Skin colour detection under changing lighting conditions," in *7th Symposium on Intelligent Robotics Systems*, (Corimbra, Portugal), July 1999.
25. M. Hiraoka, M. Firbank, M. Essenpreis, M. Cope, S. Arridge, P. van der Zee, and D. Delpy, "A Monte Carlo investigation of optical pathlength in inhomogeneous tissue and its application to near-infrared spectroscopy," *Phys. Med. Biol.* **38**, pp. 1859–1876, 1993.
26. N. Gat, "Imaging spectroscopy using tunable filters: a review," in *SPIE Conference on Algorithms for Multispectral and Hyperspectral Imagery VI*, (Orlando), April 2000.
27. R. Duda, P. Hart, and D. Stork, *Pattern Classification*, Wiley-Interscience, New York, 2 ed., 2001.
28. G. Golub and C. van Loan, *Matrix Computations*, Johns Hopkins University Press, Baltimore, MD, 1983.